Halogen-Bonding Mediated Stepwise Assembly of Gold Nanoparticles onto Planar Surfaces

Tanya Shirman, Revital Kaminker, Dalia Freeman, and Milko E. van der Boom*

Department of Organic Chemistry, The Weizmann Institute of Science, Rehovot 76100, Israel

ABSTRACT In this study halogen bonding (XB) is used as the driving force for the noncovalent assembly of gold nanoparticles (AuNPs) on silicon and quartz substrates functionalized with organic monolayers. The AuNPs are functionalized with XB-donor ligands, whereas the monolayers have pyridine groups as XB-acceptors. The surface-confined systems are formed by iteratively exposing the monolayers to solutions of organic cross-linkers having 2–4 pyridine groups and functionalized AuNPs. UV–vis spectroscopy, atomic force microscopy (AFM), and scanning electron microscopy (SEM) reveal how the structure of the resulting surface-bound assemblies are controlled by (i) the properties of the monolayers, (ii) the molecular structure and the number of XB binding sites of the organic cross-linker, and (iii) the number of functionalized AuNP and cross-linker deposition steps. Moreover, these structures exhibit surface-enhanced Raman scattering and significant changes are observed in the morphology of some of the surface-bound assemblies upon aging.

KEYWORDS: halogen bonding · nanoparticles · surface-bound assemblies · scanning electron microscopy · layer-by-layer · self assembly

Halogen bonding (XB) is a noncovalent interaction that has similarities to hydrogen bonding in terms of directionality and strength.[1–4] XB plays a significant role as a supramolecular force for forming molecular-based assemblies and has been used in crystal engineering, liquid crystals, solid-state reactions, and separation of fluoroalkanes.[5–26] In addition, XB might have biomedical importance.[27–29] Although there has been much growing interest in XB, the formation of large hybrid assemblies on surfaces has not been explored. The generation of organic compounds capable of XB with inorganic systems (*e.g.*, nanoparticles and rods, functional substrate surfaces, and metal clusters) is an interesting challenge because it might open up routes to new functional materials. Metal coordination, antigen–antibody interactions, hydrogen-bonding, and other weak interactions have already been utilized for constructing inorganic–organic assemblies based on nanoparticles, some of which exhibit properties related to sensing.[30–32]

We have recently introduced a series of XB donor–acceptor compounds that form unimolecular XB networks upon crystallization from solution (**I**–**VI**, Chart 1).[22–25] The packing and the intermolecular interactions can be controlled by systemically modifying the molecular structure, leading even to the formation of helical structures (**I**).[24] The good thermal stability and the high volatility of these compounds also permitted the formation of polycrystalline thin films by chemical vapor deposition on silicon and quartz substrates functionalized with an organic monolayer (**I**, **II**).[25]

We recently reported that functionalized AuNPs having a capping layer consisting of compound **II** (Chart 1) interact with a bifunctional XB acceptor (**BPEB**) in solution to afford supramolecular assemblies (Scheme 1A).[26] The level and morphology of the final aggregates can be controlled by varying the reaction time, whereas the degree of colloidal association is a function of the concentration of **BPEB**. Apparently XB is an excellent tool for the controlled formation of hybrid structures in solution; however, formation of surface-confined structures is desirable for further utilization and is of fundamental interest. Various methodologies have been used to attach NPs onto substrate surfaces through specific and selective noncovalent interactions.[33–36] These methods often involve chemically modifying the substrate surface with organic monolayers to bind and organize the NPs.

We demonstrate here the ability of XB to drive the stepwise assembly of functionalized AuNPs on organic monolayers. Our assembly strategy is shown in Scheme 1B. Two monolayers covalently attached to silicon and quartz substrates were used to study the effectiveness of XB in the presence (**M1**) and absence (**M2**) of other significant electrostatic interactions. Surface-confined assemblies were formed by alternately immersing the functionalized quartz and silicon substrates into a solution of

* Address correspondence to milko.vanderboom@weizmann.ac.il.

Received for review May 25, 2011 and accepted July 12, 2011.

Published online July 12, 2011
10.1021/nn201923q

Chart 1. Selection of XB Donor–Acceptor Compounds Used for Crystal Engineering, Thin Film Formation, and Assembly of AuNPs.[22–26]

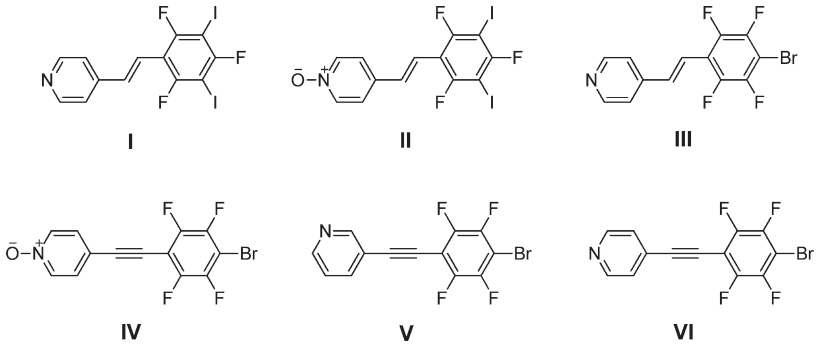

AuNP-1 (steps i and iii) and a solution of an organic cross-linker (**BPEB**, **TPEB**, or **TPM**; step ii). Both **BPEB** and **TPEB** have an essential 2D structure with potentially two and four available sites for XB, whereas **TPM** has a tetrahedral (3D) geometry with four active sites. These cross-linkers are known to control the physicochemical properties of supramolecular hybrid structures.[32,37–40] The suface-confined XB-based assemblies have been characterized by combining optical transmission (UV–vis) and Raman spectroscopy, semicontact atomic force microscopy (AFM), and scanning electron microscopy (SEM). Large amorphous spherical aggregates and small crystals became apparent upon increasing the number of deposition steps. The assemblies undergo significant structural changes during and after the stepwise deposition of **AuNP-1** and one of the cross-linkers (**BPEB**, **TPEB**, and **TPM**).

RESULTS AND DISCUSSION

Formation of Monolayers M1 and M2. Quartz and silicon substrates functionalized with a *p*-chlorobenzyl-terminated monolayer were reacted at elevated temperatures with dry solutions of (*E*)-1,2-di(pyridin-4-yl)ethane or (*E*)-4-(2-(pyridin-4-yl)vinyl)phenol for several days under an inert atmosphere to generate monolayers **M1** or **M2**, respectively (Supporting Information, Scheme S1). *p*-Chlorobenzyl and structurally related interfaces have been reported to react readily with phenol or pyridine moieties to form ether linkages or pyridinium salts, respectively.[41–46] The new monolayers (**M1**, **M2**) strongly adhere to the substrate surfaces, as demonstrated by their insolubility in common organic solvents during sonication, and their resistance to removal from the surfaces by transparent tape and CO_2 snow jet cleaning.[47] The monolayers were characterized by AFM, UV–vis spectrometry, ellipsometry, and X-ray photoelectron spectroscopy (XPS) measurements (see the Supporting Information for details). Semicontact AFM measurements revealed that both **M1** and **M2** have a smooth film surface with a root-mean-square surface roughness (R_{rms}) of 0.15–0.2 nm for scan areas of 1 μm × 1 μm with no evident grain boundaries (Supporting Information, Figures S1 and S2). The film thickness derived from ellipsometric measurements is estimated to be 1.0 nm (**M1**) and 1.2 nm (**M2**). These values are in good agreement with data reported for structurally related stilbene-based monolayers.[48] XPS measurements of monolayer **M1** grafted on Si(100) revealed a signal at 402.9 eV, indicating the formation of pyridinium salts.[48,49] The XPS measurements of monolayer **M2** also showed the presence of pyridinium salts but as a minor component (<12%). The yield of both surface functionalization processes was estimated to be 60–70%, as indicated by the presence of unreacted benzyl-chloride moieties. The yields of these and related coupling reactions are limited by steric constraints.[49,50] The benzyl halide interfaces consist of densely packed relatively small molecules and, therefore, they cannot bind quantitatively larger compounds. The UV–vis spectra of the monolayers exhibit charge-transfer bands at λ = 323 nm (**M1**) and λ = 405 nm (**M2**), which are significantly red-shifted by about 30 and 75 nm, respectively, in comparison with the absorption bands of the precursors in solution. Such large bathochromic shifts are not uncommon and can be attributed to the coupling reactions and/or a change in environment.[48,49]

Formation of AuNP-1 and AuNP-2. The NPs were functionalized with (*E*)-4 (2,3,5,6-tetrafluoro-4-iodostyryl)-pyridine-1-oxide (**1**) and (*E*)-4-(perfluorostyryl)-pyridine-1-oxide (**2**) according to our previously reported procedure and characterized by UV–vis spectroscopy and transmission electron microscopy (TEM).[26] **AuNP-1** and **AuNP-2** are stable under the reaction conditions used for the formation of the surface-confined assemblies (*vide infra*). UV–vis spectroscopy showed for both systems a typical surface plasmon band at λ_{max}= 522 nm (THF).[26,51] TEM analysis indicated an average nanoparticle diameter of 5.5 ± 0.6 nm. We have previously shown that AuNPs functionalized with (*E*)-4-(2,4,6-trifluoro-3,5-diiodostyryl)pyridine (Chart 1, **II**) slowly aggregate.[26] The new **AuNP-1** (having only one Ar_F–I moiety) is more stable toward aggregation. TEM images of **AuNP-1** aged for 24 h in THF showed that the particles remain separated (Supporting

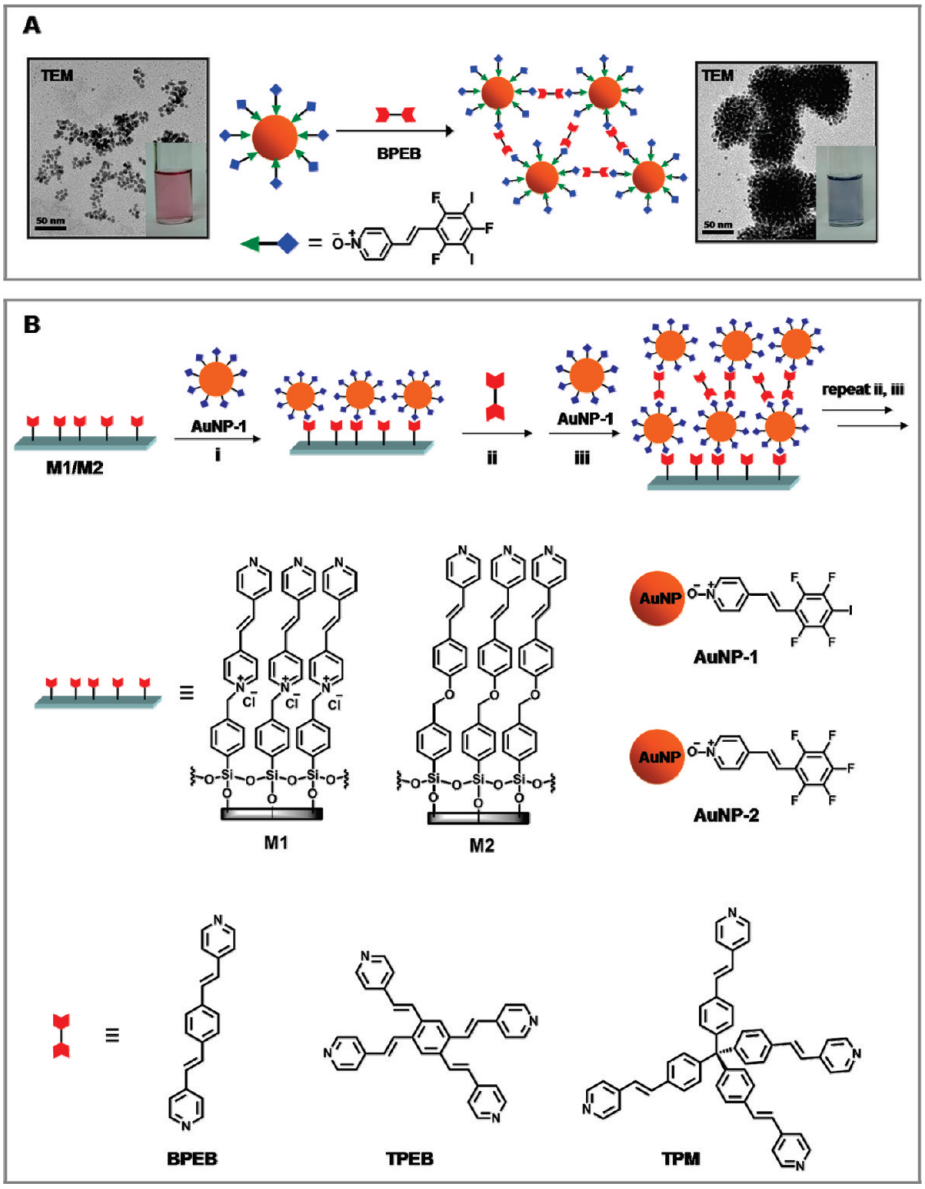

Scheme 1. (A) The formation of assemblies consisting of functionalized AuNPs and organic cross-linkers (BPEB) in solution.[26] (B) Schematic presentation of the stepwise generation of assemblies consisting of functionalized gold nanoparticles (AuNP-1) and organic cross-linkers (BPEB, TPEB, and TPM) on organic monolayers (M1, M2). For all data the last deposition step is of the functionalized AuNPs.

Information, Figure S3). **AuNP-2** does not aggregate for at least several weeks.

Selective Immobilization of AuNP-1 and AuNP-2 on layers M1 and M2. The role of the electrostatic interactions induced by the pyridinium salts *versus* XB interactions was revealed by reacting monolayers **M1** and **M2** with **AuNP-1** and **AuNP-2**. Monolayer **M1** or **M2** was immersed into a THF solution of **AuNP-1** or **AuNP-2** for 30 min (Scheme 1B, step i). Then, the functionalized substrates were washed and sonicated with THF for 3 min. Tapping mode AFM measurements showed that the AuNPs of **AuNP-1/M1** and **AuNP-2/M1** are uniformly distributed and have a narrow size distribution (15−20 nm). The TEM-derived values are smaller (5.5 ± 0.6 nm). This difference is due to convolution effects by the AFM tip.[52,53] Section analyses of AFM data show particle heights that are nearly identical to the TEM values. The SEM measurements show a diameter of ~6 nm and a surface coverage of 90% for both systems (Figure 1A−D). The surface-bound assemblies cannot be removed by repeated rinsing with THF or by sonication as judged by UV−vis spectroscopy and AFM measurements. The formation of **AuNP-2/M1** cannot involve XB. Apparently, the pyridinium salt is the dominant factor in forming the layers of AuNPs with similar morphologies for both systems (**AuNP-1**, **AuNP-2**) on monolayer **M1.**

Interestingly, the AFM and SEM analyses of the depositions of **AuNP-1** and **AuNP-2** on monolayer

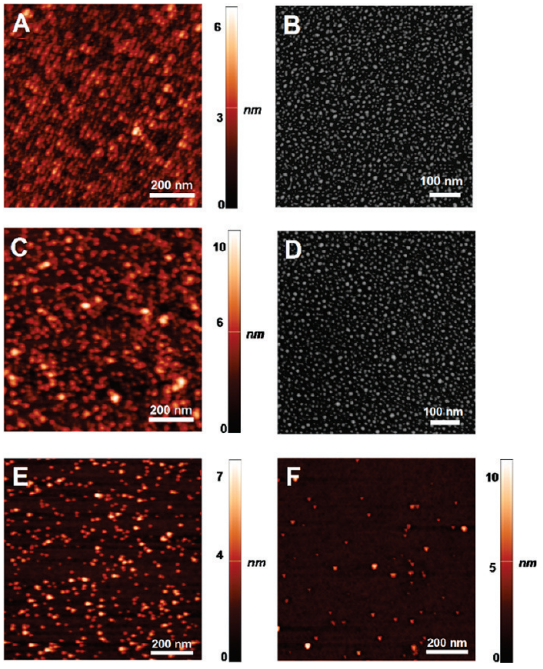

Figure 1. Representative (A) AFM (1 μm × 1 μm, R_{rms} = 0.8 nm) and (B) SEM images of AuNP-1 assembled on silicon substrates functionalized with monolayer M1. (C) AFM (1 μm × 1 μm, R_{rms} = 1.5 nm) and (D) SEM images of AuNP-2 assembled on silicon substrates functionalized with monolayer M1. Representative AFM images (1 μm × 1 μm) of (E) AuNP-1 and (F) AuNP-2 assembled on silicon substrates functionalized with monolayer M2.

M2 revealed a lower and different AuNP coverage (*i.e.*, ~50% for **AuNP-1** and <1% for **AuNP-2** by SEM; Figure 1E,F). AuNP aggregation was not observed. The AFM-derived roughness ($R_{rms} \approx 0.18$ nm) for the voids between the AuNPs corresponds to the roughness of the monolayers (**M1** or **M2**). **AuNP-2/M2** cannot involve XB. Therefore, the significantly higher AuNP coverage for **AuNP-1/M2** *versus* **AuNP-2/M2** illustrates the XB-driven selectivity (Figure 1E,F). A comparison of AFM and SEM data is shown in the Supporting Information, Table S1.

According to observations with these four systems, the presence of electrostatic interactions caused by the pyridinium salts can dominate and mask the specificity induced by XB interactions. However, the importance of XB becomes apparent when other strong intermolecular interactions are absent. We have previously shown that the structure of crystalline films formed by physical vapor deposition (PVD) can be controlled by XB between organic monolayers and the molecular components.[25]

Stepwise Formation of Surface-Bound Assemblies with AuNP-1 and Cross-Linkers (BPEB, TPEB, TPM) on Organic Monolayers (M1, M2). Iterative immersion of quartz and silicon substrates functionalized with monolayers **M1** and **M2** in freshly prepared solutions of **AuNP-1** and solutions of a cross-linker (**BPEB**, **TPEB**, or **TPM**) resulted in the formation of six assemblies where the structure is

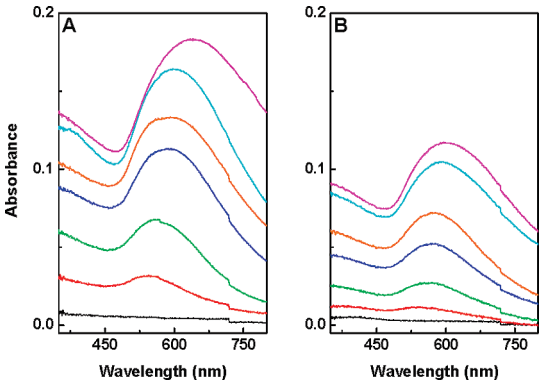

Figure 2. Representative UV−vis absorption spectra of AuNP-1/TPM assembled on quartz substrates functionalized with monolayer M1 (A) and M2 (B) for 6 AuNP-1 deposition steps.

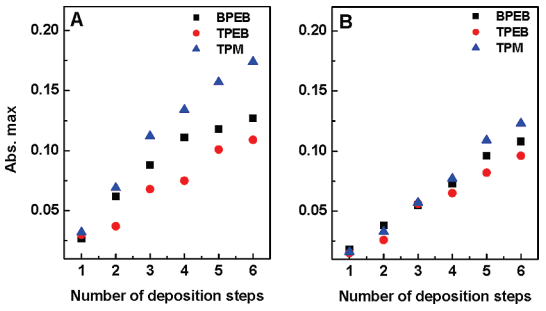

Figure 3. UV−vis absorption maxima *versus* the number of AuNP deposition steps of AuNP-1/BPEB (black), AuNP-1/TPEB (red), and AuNP-1/TPM (blue) on quartz substrates functionalized with monolayers M1 (A) and M2 (B).

dependent on the cross-linker used (Scheme 1B, steps i−iii). All deposition times are 30 min and the functionalized substrates were rinsed with THF between each step. The progress of the assembly formation is observable by the naked eye because the color of the functionalized substrates changes from red (for the first **AuNP-1** deposition step) to purple, and even to deep blue after 10 **AuNP-1** deposition steps.

The assemblies were analyzed by UV−vis spectroscopy, AFM, and SEM. *Ex-situ* UV−vis spectroscopy shows an increased intensity of the plasmon bands with the number of AuNP deposition steps and shifting of the band maxima and variations in the broadening of these bands (Figure 2). The optical data indicate that most material was assembled on the surfaces of monolayer **M1** regardless of the cross-linker used (**BPEB**, **TPEB**, **TPM**; Figure 3). This confirms the dominant role of the pyridinium salt. The absorbance intensity increases *versus* the number of **AuNP-1** depositions steps for the assemblies grown on monolayers **M1** and **M2**. The nonlinear increase for some of the assemblies might indicate incomplete coverage of AuNPs during the deposition steps and/or reflect the formation of aggregates. The optical absorption of the cross-linker (**BPEB**, **TPEB**, **TPM**) is small

in comparison to the optical absorption of the AuNPs.

Additional structural information was obtained by measuring the surface-enhanced Raman scattering (SERS) activity of **AuNP-1**/**BPEB** assembled on monolayer **M1** after 3, 6, and 8 **AuNP-1** deposition steps (Figure 4). Both **BPEB** and the AuNP capping layer (**1**) are Raman active, resulting in overlapping of some bands. Nevertheless, various groups can be identified. For instance, the band around 1180 cm^{-1} can be attributed to the N−O stretching vibration of the capping layer (**1**).[54,55] The pyridine *N*-oxide band of compound **1** appears at ∼1220 cm^{-1}. Coordination of this moiety to the AuNP results in a shift of 12−60 cm^{-1} toward lower frequencies.[56]

Representative AFM images of the 12 assemblies generated with **AuNP-1** and **BPEB**, **TPEB**, and **TPM** on monolayers **M1** and **M2** after 3 and 6 **AuNP-1** deposition steps are shown in Figure 5. The three assemblies formed on monolayer **M1** consist of small segregated areas of agglomerated colloids after three **AuNP-1** deposition steps (Figure 5, row 1). **AuNP-1**/**TPM** forms a relatively dense, uniform film on monolayer **M1** with an R_{rms} of ∼2.5 nm. **AuNP-1**/**BPEB** and **AuNP-1**/**TPEB** have a similar surface morphology, density, and roughness (R_{rms} = 3−4 nm). Apparently, the molecular geometry (2D *versus* 3D) of the cross-linker is more important than the number of binding sites (**BPEB**, 2; or **TPEB** and **TPM**, 4) in controlling the assembly structure. The morphology of **AuNP-1**/**BPEB**, **AuNP-1**/**TPEB**, and **AuNP-1**/**TPM** after six **AuNP-1** depositions is characterized by large, continuous regions of aggregated nanoparticles forming interconnected networks (Figure 5, row 2). Interestingly, the assemblies generated on monolayer **M2** have different surface morphologies (Figure 5, rows 3 and 4). After 3 **AuNP-1** depositions the surface of monolayer **M2** is covered with grainy films showing relatively large domains and a roughness of 6−7 nm. However, the coverage is somewhat higher for **AuNP-1**/**TPM**. Apparently, the different monolayer properties of **M1** and **M2** are expressed in the formation and structure of the entire assemblies.

The aggregation of the AuNPs becomes more pronounced after six **AuNP-1** deposition steps. The morphology is not only controlled by the monolayer (**M1** or **M2**). The grain size is also a function of the cross-linker: **AuNP-1/TPM** (d = 60−80 nm, h = 20−30 nm) > **AuNP-1/BPEB** (d = 35−55 nm, h = 16−20 nm) > **AuNP-1/TPEB** (d = 25−30 nm, h = 12−18 nm). These observations are in agreement with SEM analyses. Representative SEM images of the 12 assemblies generated with **AuNP-1** and **BPEB**, **TPEB**, and **TPM** on monolayers **M1** and **M2** after three and six **AuNP-1** deposition steps are shown in Figure 6.

The SEM analyses of **AuNP-1**/**BPEB**, **AuNP-1**/**TPEB**, and **AuNP-1**/**TPM** grown on monolayer **M1** show

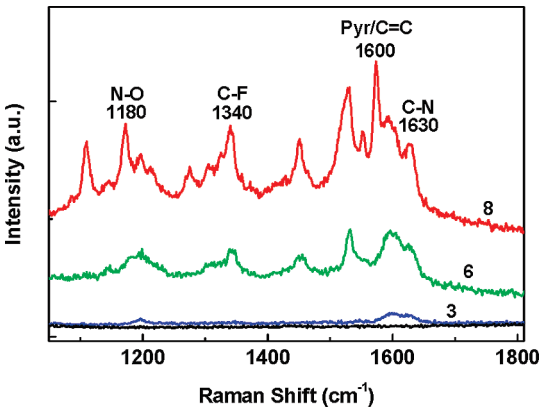

Figure 4. Representative Raman scattering spectra of AuNP-1/BPEB formed on silicon substrates functionalized with monolayer M1. The black line represents the spectrum of monolayer M1, whereas the blue, green, and red spectra were recorded after 3, 6, and 8 AuNP-1 deposition steps, respectively.

networks of densely packed and aggregated NPs. Progressively significant particle aggregation with increasing assembly steps have been previously demonstrated with other systems.[57,58] For instance, the stepwise formation of self-assembled organic/inorganic films based on multivalent host−guest interactions between dendrimers and AuNPs was demonstrated by Reinhoudt, Huskens and co-workers.[57] The SEM images of the above-mentioned three assemblies on monolayer **M2** after three and six **AuNP-1** deposition steps reveal the presence of strikingly different structures. The formation of relatively large clusters was observed on monolayer **M2** after six **AuNP-1** deposition steps. These results are in good agreement with the AFM measurements (Figure 5; row 4) and indicate that the morphology of the assemblies is highly dependent on the structure formed after the first **AuNP-1** deposition, which in turn, strongly depends on the structure of the monolayer (**M1** or **M2**). The deposition of **AuNP-1** on monolayer **M1** results in a dense layer (*vide infra*) promoting film growth mainly in the z direction. The less densely packed layer generated from the deposition of **AuNP-1** on monolayer **M2** might also induce film growth parallel to the surface (Figure 1). A comparison of AFM and SEM data of the **AuNP-1** and **AuNP-2** based assemblies is shown in the Supporting Information, Table S2.

Interestingly, the NPs do not form a network on monolayer **M2** upon increasing the number of deposition steps but rather are interaggregated and form separate clusters and grains (Figure 7). These effects are clearly observable after six AuNP deposition steps. SEM images of **AuNP-1/BPEB** and **AuNP-1/TPM** formed on monolayer **M2** reveal, after eight **AuNP-1** deposition steps, the formation of faceted crystals with well-defined shapes (triangles, hexagons) and small amounts of amorphous spherical aggregates (Figure 7A,C). **AuNP-1/TPEB** consists of mainly

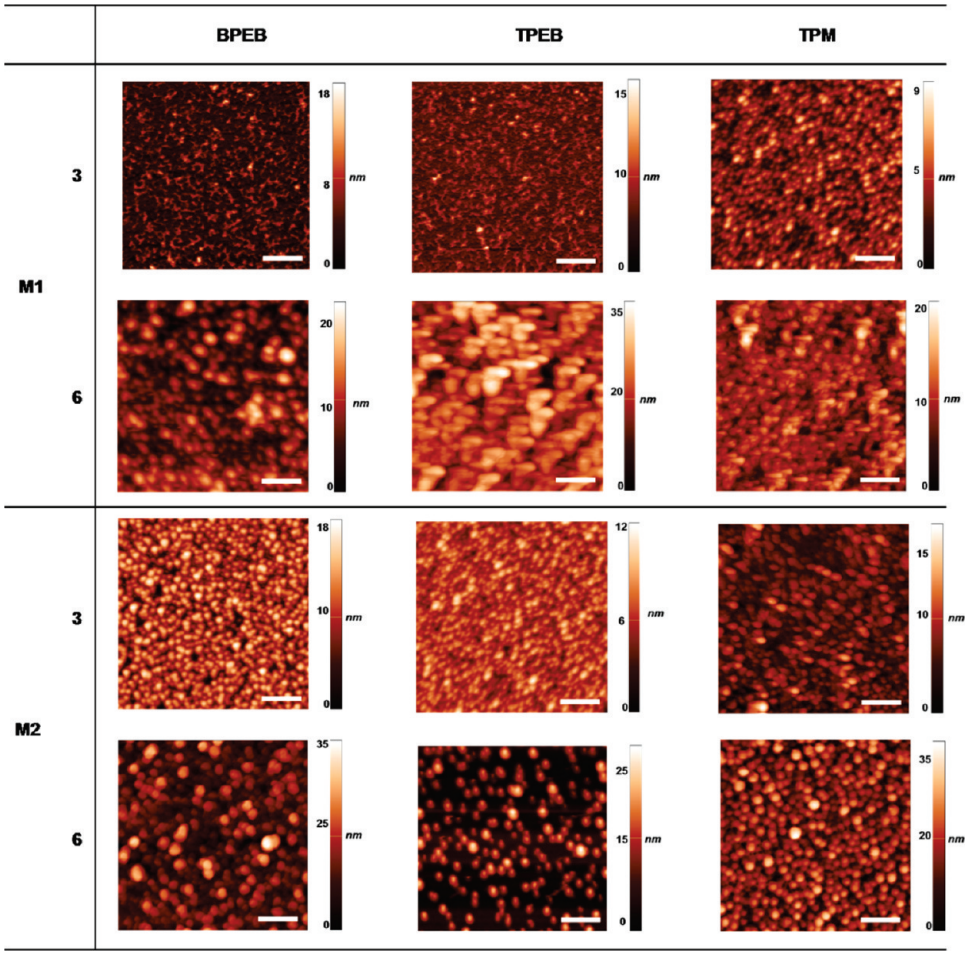

Figure 5. Representative AFM images showing scan areas of 1 μm $\times$ 1 μm of AuNP-1/BPEB, AuNP-1/TPEB, and AuNP-1/TPM after three and six AuNP-1 deposition steps, respectively. These assemblies were formed on silicon substrates functionalized with monolayers M1 and M2. The white scale bar = 200 nm.

spherical amorphous aggregates (~200 nm in diameter) consisting of smaller clusters (Figure 7B). These large aggregates consist of individual assemblies of grains and NPs similar to the ones present on the substrate surface (Figure 7B, inset). Smaller spheres were observed starting from the third AuNP deposition step. The mechanism underlying the formation and composition of these aggregates and crystals is not clear. One possible explanation for the formation of the crystals is the loss of the capping layer followed by the fusion of AuNPs.[59−61] The AuNPs are stable in solution during the assembly procedure as judged by TEM (Supporting Information, Figure S1) and were refreshed every two deposition steps. However, we cannot rigorously exclude the possibility of a solution and/or an assembly process occurring at the solid−liquid interface. Additional SEM images of various assemblies are presented in the Supporting Information (Figures S4−S8).

The importance of XB for the stepwise formation of the assemblies was demonstrated in the following control experiments. Monolayers **M1** and **M2** were exposed to solutions of **AuNP-2** and **BPEB** in an alternating fashion and the resulting assemblies were analyzed by UV−vis spectroscopy, AFM, and SEM (Figure 8 and Supporting Information Figures S9 and S10). The UV−vis measurements showed that there was no additional **AuNP-2/BPEB** bound to monolayer **M1** after the second **AuNP-2** deposition step (Figure 8A). Moreover, the growth of **AuNP-2/BPEB** on monolayer **M2** is arrested after the first **AuNP-2** deposition step (Figure 8B). In addition, the amount of material deposited on monolayer **M2** is an order of magnitude lower than on monolayer **M1**, which reflects the importance of the electrostatic interactions induced by the pyridinium salts. These results are fully in agreement with our studies on the supramolecular assembly of AuNPs mediated by XB in solution.[26] No aggregation was observed upon addition of **BPEB** to the solution of **AuNP-2**, whereas the reaction of **BPEB** with **AuNP-1** resulted in rapid formation of large assemblies (Scheme 1A). The significance of XB for the formation of the surface-confined assemblies is further evident from AuNP deposition experiments without the cross-linkers (**BPEB**, **TPEB**, or **TPM**). For instance, deposition of **AuNP-1** on **M2** results first in the binding of **AuNP-1** on

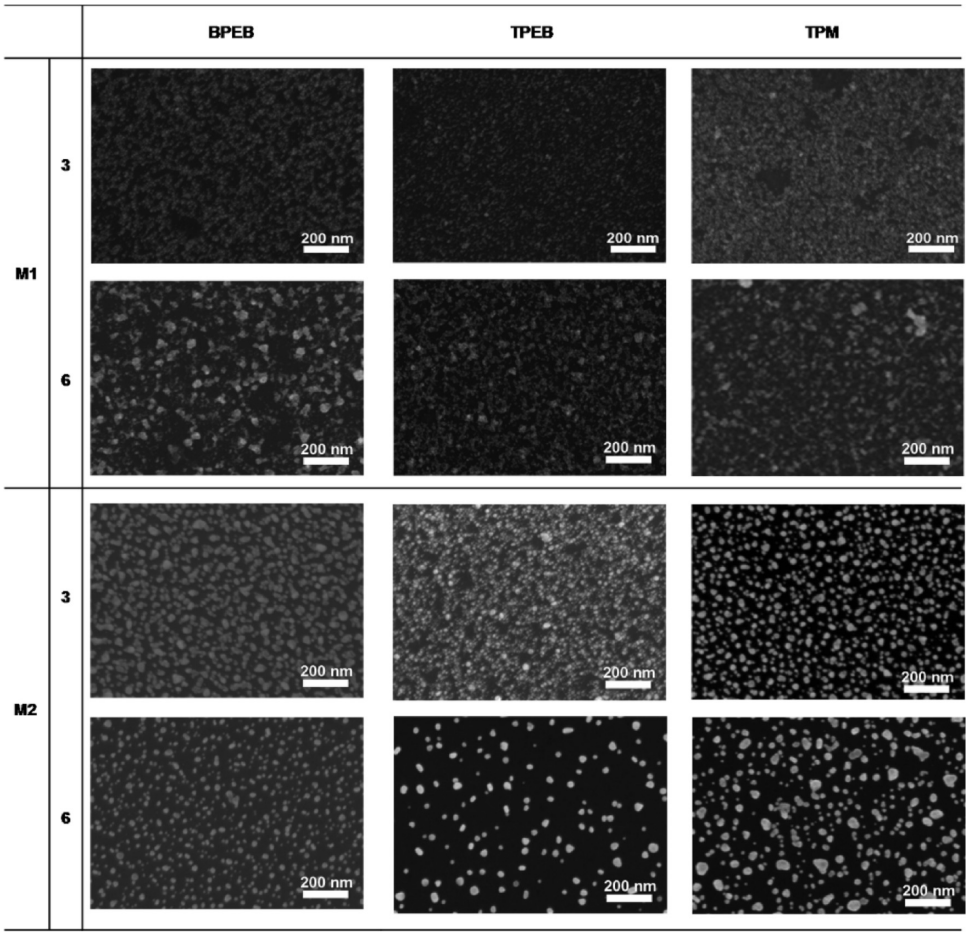

Figure 6. Representative SEM micrographs of AuNP-1/BPEB, AuNP-1/TPEB, and AuNP-1/TPM after three and six AuNP-1 deposition steps, respectively. These assemblies were formed on silicon substrates functionalized with monolayer M1 and M2. The white scale bar = 200 nm.

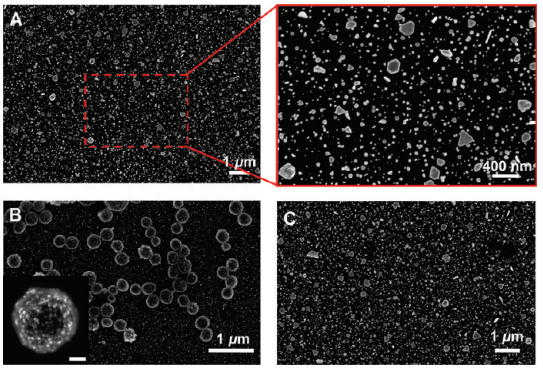

Figure 7. Representative SEM micrographs of (A) AuNP-1/BPEB, (B) AuNP-1/TPEB, and (C) AuNP-1/TPM after eight AuNP-1 deposition steps. These assemblies were formed on silicon substrates functionalized with monolayer M2. The white scale bar of the inset (B) is 200 nm.

the monolayer surface. However, no further absorption increase is observed by UV–vis spectroscopy after a second deposition of **AuNP-1**.

We found that our XB assemblies are kinetic structures that undergo structural changes on the surface in time. This aging is apparent by comparing the AFM and

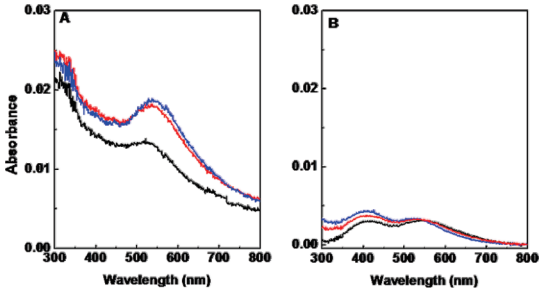

Figure 8. Representative UV–vis absorption spectra for the stepwise deposition of AuNP-2/BPEB on quartz substrates functionalized with monolayers M1 (A) and M2 (B). The (i) black, (ii) red, and (iii) blue spectra correspond to the number (1, 2, and 3) of AuNP-2 deposition steps, respectively.

SEM data from a freshly prepared **AuNP-1/BPEB** assembly on monolayer **M1** after six **AuNP-1** deposition steps with data obtained after one month (Figure 9). The assemblies were stored during this period under ambient conditions with the exclusion of light. The freshly prepared **AuNP-1/BPEB** consists of a homogeneously distributed network of aggregated nanoparticles with R_{rms} = 8 nm, whereas the aged assembly

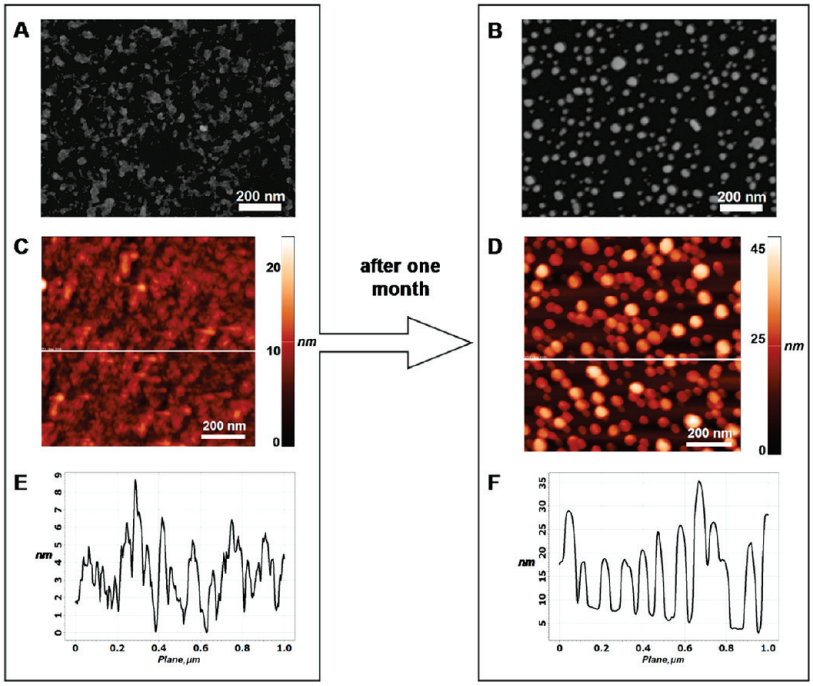

Figure 9. Representative SEM micrographs of (A) freshly prepared AuNP-1/BPEB on a silicon substrate functionalized with monolayer M1 after 6 AuNP-1 deposition steps. (B) The same AuNP-1/BPEB system after 30 days. Corresponding AFM images (C and D) and representative cross sections (E and F). The locations of the cross sections are denoted by the white lines in the AFM images.

consists of grains with a diameter of ~46 nm and a height of ~25 nm. These significant morphological changes demonstrate that the assembled AuNPs undergo a self-reorganization process at room temperature, yielding a thermodynamically more favorable structure. Rearrangement of surface-confined NPs under electric and magnetic fields, or by other stimuli has been demonstrated.[30,62−65]

SUMMARY AND CONCLUSIONS

We have demonstrated for the first time the assembly of hybrid organic−AuNP structures onto planar functionalized surfaces mediated by halogen bonding. The systems' properties are a function of (i) the monolayer properties, (ii) the molecular structure of the organic cross-linker, (iii) the number of deposition steps, and (iv) time (aging). The here reported assemblies have been prepared under identical reaction conditions. Other experimental parameters, including temperature, solvent polarity, and concentrations are likely to affect the structure of the assemblies as well. Selectivity is observed for the surface attachment of AuNPs by XB in the absence of other strong electrostatic interactions, whereas dominant electrostatic interactions resulting from salt-type monolayer structures suppress this selectivity. The morphology of the assemblies can be controlled by varying the structure of the organic cross-linker. It appears that a 2D *versus* a 3D molecular geometry has a more pronounced effect on the assembly structure than the number of coordination sites. The surface morphology undergoes drastic changes upon increasing the number of AuNP deposition steps. These changes include the formation of larger aggregates, but also the formation of faceted crystals with well-defined shapes. The aging experiments reveal that the assemblies are kinetic products that undergo significant postdeposition structural changes with time. Our findings indicate that the formation of structurally well-defined and task-specific nanoparticle-based assemblies based on XB is a realistic possibility.

EXPERIMENTAL SECTION

Materials and Methods. *m*-Chloroperbenzoic acid (mCPBA), tetraoctylammonium bromide (TOAB), sodium borohydride, (*p*-chloromethyl)phenyltrichlorosilane, and (*E*)-1,2-di(pyridin-4-yl)-ethane were obtained from Aldrich and used as received. Sodium tetrachloroaurate(III) dihydrate was purchased from ABCR GmbH & Co. Solvents (AR grade) were purchased from Bio-Lab (Jerusalem), Frutarom (Haifa), or Mallinckrodt Baker (Phillipsburg, NJ). THF was dried by distillation from sodium. Pentane and toluene were dried and purified using an M. Braun solvent purification system. Compounds (*E*)-4-(2,3,5,6-tetrafluoro-4-iodostyryl)pyridine1-oxide (**1**),[22,25,66−70] (*E*)-4-(perfluorostyryl)-pyridine 1-oxide (**2**),[22,71] 1,4-bis((*E*)-2-(pyridin-4-yl)vinyl)benzene (**BPEB**),[72,73] 1,2,4,5-tetrakis-[4-vinylpyridine]-benzene (**TPEB**),[39,73] tetrakis(4-((*E*)-2-(pyridin-4-yl)

vinyl)-phenyl) methane (**TPM**),[74] and (*E*)-4-(2-(pyridin-4-yl)vinyl) phenol[73] were prepared according to published procedures. All glassware for AuNP formation was cleaned by immersion in a piranha solution (7:3 v/v, H_2SO_4/30% H_2O_2) for 10 min, followed by washing with deionized (DI) water. Tetraoctylammonium bromide (TOAB)-capped gold nanoparticles (**AuNP-TOAB**) were prepared in toluene using the biphasic reduction method, and the subsequent TOAB capping layer exchange with ligands **1** and **2** was carried out according to a reported procedure.[26]

Single-crystal silicon (100) substrates were purchased from Wafernet (San Jose, CA) and were cleaned by sonication in hexane followed by acetone, then ethanol, and finally dried under an N_2 stream. Subsequently, they were cleaned for 20 min with UV and ozone in a UVOCS cleaning system (Montgomery, PA). Quartz substrates (Chemglass, Inc.) were cleaned by immersion in a "piranha" solution (7:3 (v/v) H_2SO_4/30% H_2O_2) for 1 h. (*Caution: piranha solution is an extremely dangerous oxidizing agent and should be handled with care using appropriate personal protection.*) Subsequently, the substrates were rinsed with deionized (DI) water followed by the RCA cleaning protocol: 1:5:1 (v/v) NH_4OH/H_2O/30% H_2O_2 at room temperature for 45 min. The substrates were washed with ample amounts of DI water and thereafter were dried under an N_2 stream. Finally, all substrates were then dried in an oven for 2 h at 130 °C.

UV−vis spectra were recorded on a Cary 100 spectrophotometer in double beam transmission mode. Transmission electron microscopy (TEM) samples were prepared by depositing a drop of the solution on freshly glow-discharged 400-mesh carbon-coated grids. The samples were observed using a Philips (FEI-Company, Holland) CM120 TEM operating at 120 KV. The images were obtained using a Gatan (Gatan USA) UltraScan 1000 2k × 2k CCD camera. AFM images were recorded using a Solver P47 (NT-MDT, Russia) operating in semicontact mode. Angle-resolved X-ray photoelectron spectra (AR-XPS) were recorded at different takeoff angles with a PHI 5600 Multi Technique System (base pressure of the main chamber 2 × 10^{-10} Torr). Spectroscopic ellipsometry was recorded on an M 2000 V (J. A. Wollam Co., Inc.) instrument with VASE32 software. High-resolution scanning electron microscope (HRSEM) imaging was carried out with a LEO-Supra 55 VP HRSEM. Raman scattering experiments were conducted by employing a Micro-Raman Renishaw InVia system with laser excitation at 632.8 (25 mW). The laser was directed through an imaging microscope having a Leica microscope magnification ranging from ×5 to ×100. The control was performed using PC base Wire II by Renishaw, Gloucestershire (UK) software.

Formation of Monolayers M1 and M2. A siloxane-based coupling layer (CL)[42,44−46,51,71] was prepared on freshly cleaned float quartz and Si(100). Substrates were treated with a dry toluene solution of (*p*-chloromethyl)phenyltrichlorosilane (1:100, v/v) at room temperature for 30 min under N_2. The substrates were then thoroughly washed with copious amounts of dry toluene and dried at 130 °C for about 15 min. Monolayer **M1** was prepared by immersing the functionalized substrates into a 2.0 mM THF solution of (*E*)-1,2-di(pyridin-4-yl)ethane, and heating for 48 h at 85 °C under N_2 in a glass pressure tube. Monolayer **M2** was prepared by heating the functionalized substrates for 3 days at 80 °C under N_2 in a 2.0 mM toluene/CH_3CN (1:1, v/v) solution of (*E*)-4-(2-(pyridin-4-yl)vinyl)phenol. The monolayers **M1** and **M2** were washed and sonicated (3 min) with copious amounts of CH_2Cl_2, acetone, and isopropyl alcohol, and dried under N_2 (Supporting Information, Scheme S1).

Formation of AuNP-Based Assemblies on Monolayers M1 and M2. The functionalized quartz and silicon substrates (**M1** or **M2**) were fully immersed in freshly prepared solutions of **AuNP-1** or **AuNP-2** (THF, ∼30 nM) followed by reacting with a THF solution of **BPEP**, **TPEB**, or **TPM** (1 mM). The reaction time of each step was 30 min and was followed by thorough rinses of the samples with THF. The AuNP deposition steps were repeated eight times. Monolayers **M1** and **M2** were added to the different solutions of AuNP and cross-linkers (**BPEP**, **TPEB**, or **TPM**). In addition, in every two deposition steps freshly prepared solutions of AuNP were used in order to avoid cross-contamination and the possible formation of aggregates.

Acknowledgment. This research was supported by the Helen and Martin Kimmel Center for Molecular Design and by the United States−Israel Binational Science Foundation (BSF). The transmission and scanning electron microscopy studies were conducted at the Irving and Cherna Moskowitz Center for Nano and Bio-Nano Imaging at the Weizmann Institute of Science. X-ray photoelectron spectroscopy (XPS) measurements were performed at the Department of Chemical Research Support by T. Bendikov and H. Cohen. M. E. van der Boom is the incumbent of the Bruce A. Pearlman Professorial Chair in Synthetic Organic Chemistry.

Supporting Information Available: Scheme S1 shows the formation of the template layers **M1** and **M2**. Additional characterization data (AFM, SEM) is available in Figures S1−S9 and Tables S1 and S2. This material is available free of charge *via* the Internet at http://pubs.acs.org.

REFERENCES AND NOTES

1. *Halogen Bonding: Fundamentals and Applications*, 1st ed.; Metrangolo, P.; Resnati, G., Eds.; Springer: New York, January 2008.
2. Metrangolo, P.; Neukirch, H.; Pilati, T.; Resnati, G. Halogen Bonding Based Recognition Processes: A World Parallel to Hydrogen Bonding. *Acc. Chem. Res.* **2005**, *38*, 386–395.
3. Politzer, P.; Murray, J. S.; Clark, T. Halogen Bonding: An Electrostatically-Driven Highly Directional Noncovalent Interaction. *Phys. Chem. Chem. Phys.* **2010**, *12*, 7748–7757.
4. Metrangolo, P.; Resnati, G. Halogen *versus* Hydrogen. *Science* **2008**, *321*, 918–919.
5. Metrangolo, P.; Meyer, F.; Pilati, T.; Resnati, G.; Terraneo, G. Halogen Bonding in Supramolecular Chemistry. *Angew. Chem., Int. Ed.* **2008**, *47*, 6114–6127.
6. Cavallo, G.; Metrangolo, P.; Pilati, T.; Resnati, G.; Sansotera, M.; Terraneo, G. Halogen Bonding: A General Route in Anion Recognition and Coordination. *Chem. Soc. Rev.* **2010**, *39*, 3772–3783.
7. Espallargas, G. M.; Zordan, F.; Marín, L. A.; Adams, H.; Shankland, K.; van de Streek, J.; Brammer, L. Rational Modification of the Hierarchy of Intermolecular Interactions in Molecular Crystal Structures. *Chem.—Eur. J.* **2009**, *15*, 7554–7568.
8. Caballero, A.; White, N. G.; Beer, P. D. A Bidentate Halogen-Bonding Bromoimidazoliophane Receptor for Bromide Ion Recognition in Aqueous Media. *Angew. Chem., Int. Ed.* **2011**, *50*, 1845–1848.
9. Brezgunova, M.; Shin, K.-S.; Auban-Senzier, P.; Jeannin, O.; Fourmigué, M. Combining Halogen Bonding and Chirality in a Two-Dimensional Organic Metal (EDT-TTF-I_2)$_2$(*D*-camphorsulfonate)·H_2O. *Chem. Commun.* **2010**, *46*, 3926–3928.
10. Vartanian, M.; Lucassen, A. C. B.; Shimon, L. J. W.; van der Boom, M. E. Cocrystallization of a Tripyridyl Donor with Perfluorinated Iodobenzene Derivatives: Formation of Different N···I Halogen Bonds Determining Network *vs* Plain Packing Crystals. *Cryst. Growth Des.* **2008**, *8*, 786–790.
11. Aragoni, M. C.; Arca, M.; Devillanova, F. A.; Hursthouse, M. B.; Huth, S. L.; Isaia, F.; Lippolis, V.; Mancini, A.; Verani, G. Reactions of Halogens/Interhalogens with Polypyridyl Substrates: The Case of 2,4,6-Tris(2-pyridyl)-1,3,5-triazine. *Eur. J. Inorg. Chem.* **2008**, 3921–3928.
12. Halogen bonding is of much theoretical interest. For an example of a combined experimental and computational study, see: Roper, L. C.; Präsang, C.; Kozhevnikov, V. N.; Whitwood, A. C.; Karadakov, P. B.; Bruce, D. W. Experimental and Theoretical Study of Halogen-Bonded Complexes of DMAP with Di- and Triiodofluorobenzenes. A Complex with a Very Short N···I Halogen Bond. *Cryst. Growth Des.* **2010**, *10*, 3710–3720.
13. Rissanen, K. Halogen Bonded Supramolecular Complexes and Networks. *CrystEngComm* **2008**, *10*, 1107–1113.
14. Clarke, S. M.; Friščić, T.; Jones, W.; Mandal, A.; Sun, C.; Parker, J. E. Observation of a Two-Dimensional Halogen-Bonded Cocrystal at Sub-monolayer Coverage Using Synchrotron X-ray Diffraction. *Chem. Commun.* **2011**, *47*, 2526–2528.
15. Legon, A. C. The Halogen Bond: an Interim Perspective. *Phys. Chem. Chem. Phys.* **2010**, *12*, 7736–7747.

16. Bruce, D. W.; Metrangolo, P.; Meyer, F.; Pilati, T.; Praesang, C.; Resnati, G.; Terraneo, G.; Wainwright, S. G.; Whitwood, A. C. Structure−Function Relationships in Liquid-Crystalline Halogen-Bonded Complexes. *Chem.—Eur. J.* **2010**, *16*, 9511–9524.
17. Caronna, T.; Liantonio, R.; Logothetis, T. A.; Metrangolo, P.; Pilati, T.; Resnati, G. Halogen Bonding and $\pi\cdots\pi$ Stacking Control Reactivity in the Solid State. *J. Am. Chem. Soc.* **2004**, *126*, 4500–4501.
18. Kilah, N. L.; Wise, M. D.; Serpell, C. J.; Thompson, A. L.; White, N. G.; Christensen, K. E.; Beer, P. D. Enhancement of Anion Recognition Exhibited by a Halogen-Bonding Rotaxane Host System. *J. Am. Chem. Soc.* **2010**, *132*, 11893–11895.
19. Giljohann, D. A.; Seferos, D. S.; Daniel, W. L.; Massich, M. D.; Patel, P. C.; Mirkin, C. A. Gold Nanoparticles for Biology and Medicine. *Angew. Chem., Int. Ed.* **2010**, *49*, 3280–3294.
20. Metrangolo, P.; Carcenac, Y.; Lahtinen, M.; Pilati, T.; Rissanen, K.; Vij, A.; Resnati, G. Nonporous Organic Solids Capable of Dynamically Resolving Mixtures of Diiodoperfluoroalkanes. *Science* **2009**, *323*, 1461–1464.
21. Yoon, J. K.; Son, W.-J.; Chung, K.-H.; Kim, H.; Han, S.; Kahng, S. J. Visualizing Halogen Bonds in Planar Supramolecular Systems. *J. Phys. Chem. C* **2011**, *115*, 2297–2301.
22. Lucassen, A. C. B.; Vartanian, M.; Leitus, G.; van der Boom, M. E. 4′-Bromo-2′,3′,5′,6′-tetrafluorostilbazole: Donor and Acceptor Site for Halogen Bonding and π-Stacking in One Rigid-Rod-Type Molecule. *Cryst. Growth Des.* **2005**, *5*, 1671–1673.
23. Lucassen, A. C. B.; Zubkov, T.; Shimon, L. J. W.; van der Boom, M. E. Design, Synthesis and Crystal Structure of a Multiple Donor−Acceptor Halogen Bonded Stilbazole: Assembly of Unimolecular Interconnected Helices. *CrystEngComm* **2007**, *9*, 538–540.
24. Shirman, T.; Lamère, J.-F.; Shimon, L. J. W.; Gupta, T.; Martin, J. M. L.; van der Boom, M. E. Halogen-Bonded Supramolecular Assemblies Based on Phenylethynyl Pyridine Derivatives: Driving Crystal Packing through Systematic Chemical Modifications. *Cryst. Growth Des.* **2008**, *8*, 3066–3072.
25. Shirman, T.; Freeman, D.; Posner, Y. D.; Feldman, I.; Facchetti, A.; van der Boom, M. E. Assembly of Crystalline Halogen-Bonded Materials by Physical Vapor Deposition. *J. Am. Chem. Soc.* **2008**, *130*, 8162–8163.
26. Shirman, T.; Arad, T.; van der Boom, M. E. Halogen Bonding: A Supramolecular Entry for Assembling Nanoparticles. *Angew. Chem., Int. Ed.* **2010**, *49*, 926–929.
27. Hardegger, L. A.; Kuhn, B.; Spinnler, B.; Anselm, L.; Ecabert, R.; Stihle, M.; Gsell, B.; Thoma, R.; Diez, J.; Benz, J.; et al. Systematic Investigation of Halogen Bonding in Protein−Ligand Interactions. *Angew. Chem., Int. Ed.* **2011**, *50*, 314–318.
28. Wsik, R.; Łebska, M.; Felczak, K.; Poznaski, J.; Shugar, D. Relative Role of Halogen Bonds and Hydrophobic Interactions in Inhibition of Human Protein Kinase CK2α by Tetrabromobenzotriazole and Some C(5)-Substituted Analogues. *J. Phys. Chem. B* **2010**, *114*, 10601–10611.
29. Auffinger, P.; Hays, F. A.; Westhof, E.; Ho, P. S. Halogen Bonds in Biological Molecules. *Proc. Natl. Acad. Sci. U.S.A.* **2004**, *101*, 16789–16794.
30. Grzelczak, M.; Vermant, J.; Furst, E. M.; Liz-Marzán, L. M. Directed Self-Assembly of Nanoparticles. *ACS Nano* **2010**, *4*, 3591–3605.
31. Daniel, M.-C.; Astruc, D. Gold Nanoparticles: Assembly, Supramolecular Chemistry, Quantum-Size-Related Properties, and Applications toward Biology, Catalysis, and Nanotechnology. *Chem. Rev.* **2004**, *104*, 293–346.
32. Lim, S. I.; Zhong, C.-J. Molecularly Mediated Processing and Assembly of Nanoparticles: Exploring the Interparticle Interactions and Structures. *Acc. Chem. Res.* **2009**, *42*, 798–808.
33. Shipway, A. N.; Katz, E.; Willner, I. Nanoparticle Arrays on Surfaces for Electronic, Optical, and Sensor Applications. *ChemPhysChem* **2000**, *1*, 18–52.
34. Crespo-Biel, O.; Ravoo, B. J.; Reinhoudt, D. N.; Huskens, J. Noncovalent Nanoarchitectures on Surfaces: from 2D to 3D Nanostructures. *J. Mater. Chem.* **2006**, *16*, 3997–4021.
35. Kinge, S.; Crego-Calama, M.; Reinhoudt, D. N. Self-Assembling Nanoparticles at Surfaces and Interfaces. *ChemPhysChem* **2008**, *9*, 20–42.
36. Li, X.-M.; Huskens, J.; Reinhoudt, D. N. Reactive Self-Assembled Monolayers on Flat and Nanoparticle Surfaces, and Their Application in Soft and Scanning Probe Lithographic Nanofabrication Technologies. *J. Mater. Chem.* **2004**, *14*, 2954–2971.
37. Ji, Q.; Acharya, S.; Hill, J. P.; Richards, G. J.; Ariga, K. Multi-Dimensional Control of Surfactant-Guided Assemblies of Quantum Gold Particles. *Adv. Mater.* **2008**, *20*, 4027–4032.
38. Kaminker, R.; Lahav, M.; Motiei, L.; Vartanian, M.; Popovitz-Biro, R.; Iron, M. A.; van der Boom, M. E. Molecular Structure−Function Relations of the Optical Properties and Dimensions of Gold Nanoparticle Assemblies. *Angew. Chem., Int. Ed.* **2010**, *49*, 1218–1221.
39. Wei, Y.; Bishop, K. J. M.; Kim, J.; Soh, S.; Grzybowski, B. A. Making Use of Bond Strength and Steric Hindrance in Nanoscale Synthesis. *Angew. Chem., Int. Ed.* **2009**, *48*, 9477–9480.
40. Musick, M. D.; Keating, C. D.; Lyon, L. A.; Botsko, S. L.; Pena, D. J.; Holliway, W. D.; McEvoy, T. M.; Richardson, J. N.; Natan, M. J. Metal Films Prepared by Stepwise Assembly. 2. Construction and Characterization of Colloidal Au and Ag Multilayers. *Chem. Mater.* **2000**, *12*, 2869–2881.
41. Yerushalmi, R.; Scherz, A.; van der Boom, M. E. Enhancement of Molecular Properties in Thin Films by Controlled Orientation of Molecular Building Blocks. *J. Am. Chem. Soc.* **2004**, *126*, 2700–2701.
42. Sarno, D. M.; Jiang, B.; Grosfeld, D.; Afriyie, J. O.; Matienzo, L. J.; Jones, W. E., Jr. Self-Assembled Molecular Architectures on Surfaces: New Strategies Involving Metal−Organic Copolymers. *Langmuir* **2000**, *16*, 6191–6199.
43. Li, D.; Ratner, M. A.; Marks, T. J.; Zhang, C.; Yang, J.; Wong, G. K. Chromophoric Self-Assembled Multilayers. Organic Superlattice Approaches to Thin-Film Nonlinear Optical Materials. *J. Am. Chem. Soc.* **1990**, *112*, 7389–7390.
44. Lin, W.; Lin, W.; Wong, G. K.; Marks, T. J. Supramolecular Approaches to Second-Order Nonlinear Optical Materials. Self-Assembly and Microstructural Characterization of Intrinsically Acentric [(Aminophenyl)azo]pyridinium Superlattices. *J. Am. Chem. Soc.* **1996**, *118*, 8034–8042.
45. Brandow, S. L.; Chen, M.-S.; Dulcey, C. S.; Dressick, W. J. Formation of Aromatic Siloxane Self-Assembled Monolayers. *Langmuir* **2008**, *24*, 3888–3896.
46. Gulino, A.; Mineo, P.; Scamporrino, E.; Vitalini, D.; Fragalà, I. Molecularly Engineered Silica Surfaces with an Assembled Porphyrin Monolayer as Optical NO_2 Molecular Recognizers. *Chem. Mater.* **2004**, *16*, 1838–1840.
47. Chow, B. Y.; Mosley, D. W.; Jacobson, J. M. Perfecting Imperfect "Monolayers": Removal of Siloxane Multilayers by CO_2 Snow Treatment. *Langmuir* **2005**, *21*, 4782–4785.
48. Filip-Granit, N.; Yerushalmi, R.; Brandis, A.; van der Boom, M. E.; Scherz, A. Uniform Approach to Bacteriochlorophyll-Based Monolayers on Conducting, Semiconducting, and Insulating Substrates. *J. Phys. Chem. B* **2005**, *109*, 6933–6935.
49. Koloski, T. S.; Dulcey, C. S.; Haralson, Q. J.; Calvert, J. M. Nucleophilic Displacement Reactions at Benzyl Halide Self-Assembled Monolayer Film Surfaces. *Langmuir* **1994**, *10*, 3122–3133.
50. Roscoe, S. B.; Yitzchaik, S.; Kakkar, A. K.; Marks, T. J.; Xu, Z.; Zhang, T.; Lin, W.; Wong, G. K. Self-Assembled Chromophoric NLO-Active Structures. Second-Harmonic Generation and X-ray Photoelectron Spectroscopic Studies of Nucleophilic Substitution and Ion Exchange Processes on Benzyl Halide-Functionalized Surfaces. *Langmuir* **1996**, *12*, 5338–5349.
51. Thomas, K. G.; Zajicek, J.; Kamat, P. V. Surface Binding Properties of Tetraoctylammonium Bromide-Capped Gold Nanoparticles. *Langmuir* **2002**, *18*, 3722–3727.
52. Lyon, L. A.; Pena, D. J.; Natan, M. J. Surface Plasmon Resonance of Au Colloid-Modified Au Films: Particle Size Dependence. *J. Phys. Chem. B* **1999**, *103*, 5826–5831.
53. Grabar, K. C.; Brown, K. R.; Keating, C. D.; Stranick, S. J.; Tang, S.-L.; Natan, M. J. Nanoscale Characterization of Gold

Colloid Monolayers: A Comparison of Four Techniques. *Anal. Chem.* **1997**, *69*, 471–477.
54. Muniz-Miranda, M.; Pergolese, B.; Sbrana, G.; Bigotto, A. Vibrational spectra and Molecular Structure of 4,4′-Azobis-(pyridine *N*-Oxide). *J. Mol. Struct.* **2005**, *744*, 339–343.
55. Ito, M.; Hata, N. Infrared and Raman Spectra of Pyridine *N*-Oxide. *Bull. Chem. Soc. Jpn.* **1955**, *28*, 353–355.
56. Garvey, R. G.; Nelson, J. H.; Ragsdale, R. O. The Coordination Chemistry of Aromatic Amine *N*-Oxides. *Coord. Chem. Rev.* **1968**, *3*, 375–407.
57. Crespo-Biel, O.; Dordi, B.; Reinhoudt, D. N.; Huskens, J. Supramolecular Layer-by-Layer Assembly: Alternating Adsorptions of Guest- and Host-Functionalized Molecules and Particles Using Multivalent Supramolecular Interactions. *J. Am. Chem. Soc.* **2005**, *127*, 7594–7600.
58. Chirea, M.; Pereira, C. M.; Silva, F. Catalytic Effect of Gold Nanoparticles Self-Assembled in Multilayered Polyelectrolyte Films. *J. Phys. Chem. C* **2007**, *111*, 9255–9266.
59. Shipway, A.; Lahav, M.; Gabai, R.; Willner, I. Investigations into the Electrostatically Induced Aggregation of Au Nanoparticles. *Langmuir* **2000**, *16*, 8789–8795.
60. Musick, M. D.; Pena, D. J.; Botsko, S. L.; McEvoy, T. M.; Richardson, J. N.; Natan, M. J. Electrochemical Properties of Colloidal Au-Based Surfaces: Multilayer Assemblies and Seeded Colloid Films. *Langmuir* **1999**, *15*, 844–850.
61. Kiely, C. J.; Fink, J.; Brust, M.; Bethell, D.; Schiffrin, D. J. Spontaneous Ordering of Bimodal Ensembles of Nanoscopic Gold Clusters. *Nature* **1998**, *396*, 444–446.
62. Dai, Q.; Nelson, A. Magnetically-Responsive Self Assembled Composites. *Chem. Soc. Rev.* **2010**, *39*, 4057–4066.
63. Sagara, T.; Kokubu, M. Potential-Driven Dynamic Behavior of Surface Modified Gold Nanoparticles at a Au(111) Electrode Surface. *e-J. Surf. Sci. Nanotechnol.* **2005**, *3*, 141–144.
64. Klajn, R.; Stoddart, J. F.; Grzybowski, B. A. Nanoparticles Functionalized with Reversible Molecular and Supramolecular Switches. *Chem. Soc. Rev.* **2010**, *39*, 2203–2237.
65. Peng, H.-l.; Krauss, T. D.; Miller, B. L. Aging Induced Ag Nanoparticle Rearrangement under Ambient Atmosphere and Consequences for Nanoparticle-Enhanced DNA Biosensing. *Anal. Chem.* **2010**, *82*, 8664–8670.
66. Krebs, F. C.; Jensen, T. Fluorinated Molecules Relevant to Conducting Polymer Research. *J. Fluorine Chem.* **2003**, *120*, 77–84.
67. Leroy, J.; Schollhorn, B.; Syssa-Magale, J.-L.; Boubekeur, K.; Palvadeau, P. A Convenient Preparation of 2,3,5,6-Tetrafluoro-4-iodo-benzaldehyde and its Application in Porphyrin Synthesis. *J. Fluorine Chem.* **2004**, *125*, 1379–1382.
68. Aakeroy, C. B.; Schultheiss, N.; Desper, J.; Moore, C. Attempted Assembly of Discrete Coordination Complexes into 1-D Chains using Halogen Bonding or Halogen...Halogen Interactions. *CrystEngComm* **2007**, *9*, 421–426.
69. Cymerman Craig, J.; Purushothaman, K. K Improved Preparation of Tertiary Amine *N*-Oxides. *J. Org. Chem.* **1970**, *35*, 1721–1722.
70. Nienkemper, K.; Kotov, V. V.; Kehr, G.; Erker, G.; Froehlich, R. Chelate [2-(Iminoethyl)pyridine *N*-Oxide]metal Complexes – Synthesis and Structural Comparison with Their Chemically Related 2-(Iminoethyl)pyridine-Derived Systems. *Eur. J. Inorg. Chem.* **2006**, 366–379.
71. Lorance, E. D.; Kramer, W. H.; Gould, I. R. Kinetics of Reductive N–O Bond Fragmentation: The Role of a Conical Intersection. *J. Am. Chem. Soc.* **2002**, *124*, 15225–15238.
72. Detert, H.; Stalmach, U.; Sugiono, E. Acidochromism of the Luminescence of Bis(4-pyridylethenyl)arenes. *Synth. Met.* **2004**, *147*, 227–231.
73. Amoroso, A. J.; Thompson, A. M. W. C.; Maher, J. P.; McCleverty, J. A.; Ward, M. D. Di-, Tri-, and Tetranucleating Pyridyl Ligands which Facilitate Multicenter Magnetic Exchange between Paramagnetic Molybdenum Centers. *Inorg. Chem.* **1995**, *34*, 4828–4835.
74. Choudhury, J.; Kaminker, R.; Motiei, L.; de Ruiter, G.; Morozov, M.; Lupo, F.; Gulino, A.; van der Boom, M. E. Linear vs Exponential Formation of Molecular-Based Assemblies. *J. Am. Chem. Soc.* **2010**, *132*, 9295–9297.